Publication Year	2022
Acceptance in OA	2022-06-15T10:51:57Z
Title	Retrieving the transmission spectrum of HD 209458b using CHOCOLATE: a new chromatic Doppler tomography technique
Authors	Esparza-Borges, E., Oshagh, M., Casasayas-Barris, N., Pallé, E., Chen, G., Morello, G., Santos, N. C., Seidel, J. V., SOZZETTI, Alessandro, Allart, R., Figueira, P., Bourrier, V., Lillo-Box, J., BORSA, Francesco, Zapatero Osorio, M. R., Tabernero, H., Demangeon, O. D. S., Adibekyan, V., González Hernández, J. I., Mehner, A., Allende Prieto, C., DI MARCANTONIO, Paolo, Alibert, Y., CRISTIANI, Stefano, Lo Curto, G., Martins, C. J. A. P., MICELA, Giuseppina, Pepe, F., Rebolo, R., Sousa, S. G., Suárez Mascareño, A., Udry, S.
Publisher's version (DOI)	10.1051/0004-6361/202141826
Handle	http://hdl.handle.net/20.500.12386/32325
Journal	ASTRONOMY & ASTROPHYSICS
Volume	657

A&A 657, A23 (2022)
https://doi.org/10.1051/0004-6361/202141826
© ESO 2021

Astronomy
&
Astrophysics

Retrieving the transmission spectrum of HD 209458b using CHOCOLATE: a new chromatic Doppler tomography technique[⋆]

E. Esparza-Borges[1,2], M. Oshagh[1,2], N. Casasayas-Barris[3], E. Pallé[1,2], G. Chen[4,5], G. Morello[1,2], N. C. Santos[6,7], J. V. Seidel[9], A. Sozzetti[11], R. Allart[15,9], P. Figueira[16,6], V. Bourrier[9], J. Lillo-Box[17], F. Borsa[13], M. R. Zapatero Osorio[18], H. Tabernero[6,7,18], O. D. S. Demangeon[6,7], V. Adibekyan[6,7], J. I. González Hernández[1,2], A. Mehner[16], C. Allende Prieto[1,2], P. Di Marcantonio[12], Y. Alibert[19], S. Cristiani[12], G. Lo Curto[16], C. J. A. P. Martins[6,8], G. Micela[14], F. Pepe[10], R. Rebolo[1,2,20], S. G. Sousa[6,7], A. Suárez Mascareño[1,2], and S. Udry[10]

[1] Instituto de Astrofísica de Canarias, 38200 La Laguna, Tenerife, Spain
e-mail: `alu0100966121@ull.edu.es`
[2] Departamento de Astrofísica, Universidad de La Laguna, 38206 La Laguna, Tenerife, Spain
[3] Leiden Observatory, Leiden University, Postbus 9513, 2300 RA Leiden, The Netherlands
[4] CAS Key Laboratory of Planetary Sciences, Purple Mountain Observatory, Chinese Academy of Sciences, Nanjing 210023, PR China
[5] CAS Center for Excellence in Comparative Planetology, Hefei 230026, PR China
[6] Instituto de Astrofísica e Ciências do Espaço, Universidade do Porto CAUP, Rua das Estrelas 4150-762 Porto, Portugal
[7] Departamento de Física e Astronomia Faculdade de Ciências, Universidade do Porto, Rua do Campo Alegre 687, 4169-007 Porto, Portugal
[8] Centro de Astrofísica da Universidade do Porto, Rua das Estrelas, 4150-762 Porto, Portugal
[9] Observatoire astronomique de l'Université de Genève, Chemin Pegasi 51, 1290 Versoix, Switzerland
[10] Université de Genève, Observatoire Astronomique, Chemin Pegasi 51, 1290 Versoix, Switzerland
[11] INAF – Osservatorio Astrofisico di Torino, Via Osservatorio 20, 10025 Pino Torinese, Italy
[12] INAF – Osservatorio Astronomico di Trieste, via G. B. Tiepolo 11, 34143 Trieste, Italy
[13] INAF – Osservatorio Astronomico di Brera, Via E. Bianchi 46, 23807 Merate (LC), Italy
[14] INAF – Osservatorio Astronomico di Palermo, Piazza del Parlamento 1, 90134 Palermo, Italy
[15] Department of Physics, and Institute for Research on Exoplanets, Université de Montréal, Montréal, H3T 1J4, Canada
[16] European Southern Observatory, Alonso de Córdova 3107, Vitacura, Región Metropolitana, Chile
[17] Centro de Astrobiología (CSIC-INTA), Depto. de Astrofísica, ESAC campus 28692 Villanueva de la Cañada (Madrid), Spain
[18] Centro de Astrobiología (CSIC-INTA), Carretera de Ajalvir km 4, 28850 Torrejón de Ardoz, Madrid, Spain
[19] Physics Institute, University of Bern, Sidlerstrasse 5, 3012 Bern, Switzerland
[20] Consejo Superior de Investigaciones Cientifícas, Spain

Received 19 July 2021 / Accepted 27 September 2021

ABSTRACT

Multiband photometric transit observations or low-resolution spectroscopy (spectro-photometry) are normally used to retrieve the broadband transmission spectra of transiting exoplanets in order to assess the chemical composition of their atmospheres. In this paper we present an alternative approach for recovering the broadband transmission spectra using chromatic Doppler tomography based on physical modeling through the `SOAP` tool: CHOCOLATE (CHrOmatiC line prOfiLe tomogrAphy TEchnique). To validate the method and examine its performance, we use observational data recently obtained with the ESPRESSO instrument to retrieve the transmission spectra of the archetypal hot Jupiter HD 209458b. Our findings indicate that the recovered transmission spectrum is in good agreement with the results presented in previous studies, which used different methodologies to extract the spectrum, achieving similar precision. We explored several atmospheric models and inferred from spectral retrieval that a model containing H_2O and NH_3 is the preferred scenario. The CHOCOLATE methodology is particularly interesting for future studies of exoplanets around young and active stars or moderate to fast rotating stars, considering `SOAP`'s ability to model stellar active regions and the fact that the rotational broadening of spectral lines favors its application. Furthermore, CHOCOLATE will allow the broad transmission spectrum of a planet to be retrieved using high-S/N, high-resolution spectroscopy with the next generation of extremely large telescopes, where low-resolution spectroscopy will not always be accessible.

Key words. methods: observational – methods: numerical – techniques: radial velocities – techniques: spectroscopic – planets and satellites: atmospheres

---

[⋆] Based on guaranteed time observations collected at the European Southern Observatory (ESO) under ESO program 1102.C-0744 by the ESPRESSO Consortium.

1. Introduction

During its passage in front of its rotating host star, a transiting exoplanet creates a radial velocity (RV) signal, which is generated by obstructing the Doppler-shifted components of the portion of the stellar disk that is blocked by the planet. This is known as the Rossiter–McLaughlin (RM) effect (Holt 1893; Rossiter 1924; McLaughlin 1924). The RM signal contains several important pieces of information, including the sky-projected planetary spin-orbit angle (Triaud 2018, and references therein). Similar to the depth of the photometric transit light curve, the RM semi-amplitude also scales with the square of the planet-star radius ratio (Snellen 2004). Recently, several studies employed the chromatic RM technique using HARPS, CARMENES, and ESPRESSO spectrograph data on HD 189733 and HD 209458 (Di Gloria et al. 2015; Oshagh et al. 2020; Santos et al. 2020), and they showed that it can be a powerful method for probing wide broadband features, which are challenging to probe from the ground. Moreover, Oshagh et al. (2020) demonstrated the advantage of chromatic RM analysis by combining HARPS and CARMENES observations, which covered a wide wavelength range and allowed precise estimations of the stellar active regions' properties and the mitigation of their impact on the retrieved transmission spectra.

During a transit, the planet occults different patches of the stellar surface along its trajectory, effectively removing the corresponding contribution to the stellar line profile at that local stellar velocity. Thus, the traveling Doppler shadow cast by the planet creates an identifiable distortion in the line profiles. Assessing these deformations is called line-profile tomography. This method has been very useful for successfully estimating the sky-projected planetary spin-orbit angle for planets around fast rotating host stars (e.g., Collier Cameron et al. 2010; Hartman et al. 2015; Zhou et al. 2017; Johnson et al. 2015). As for the transit's depth in photometric transit light curves, the line-profile distortions also scale with the planet-star radius ratio. Thus, measuring line-profile distortions over several wavelength bins yields a low-resolution broadband transmission spectrum of the planet atmosphere.

The chromatic RM is based on the strong dependence of the RM signal's amplitude on the planet-star radius ratio. Thus, the study of this dependence at different wavelength ranges leads to the determination of the planetary radius as a function of wavelength. Currently, Di Gloria et al. (2015), Oshagh et al. (2020), and Santos et al. (2020) have been the only studies to make use of the chromatic RM technique to retrieve transmission spectra of HD 189733b and HD 209458b.

Borsa et al. (2016) attempted, for the first time, the chromatic line-profile tomography technique on the well-known exoplanet HD 189733b using HARPS observations, obtaining results broadly consistent with other ground- and space-based observations. However, their preprocessing steps and their modeling approach were criticized by Cegla et al. (2017), who showed that it is not possible to obtain exoplanet radius measurements with ground-based observations using the methods applied in Borsa et al. (2016) due to the transit light curve normalization necessary to remove the effects of the Earth's atmosphere. The approximate model used to calculate the planet radius from the deformations in the chromatic line profiles was also called into question.

Here we present CHOCOLATE (CHrOmatiC line prOfiLe tomogrAphy TEchnique), which is an alternative method for retrieving the transmission spectrum from chromatic line-profile tomography based on physical modeling, and we validate its performance using ESPRESSO spectra of HD 209458b. HD 209458b is a hot Jupiter orbiting around a solar-type star. It was the first exoplanet detected by the transit technique (Charbonneau et al. 2000; Henry et al. 2000) and the first exoplanet whose atmosphere was detected (Charbonneau et al. 2002). Since then, several spectral features (e.g., Na, H_2O, CO, He, TiO, CH_4, HCN, NH3 and Fe+) have been detected in the atmosphere of HD 209458b (Snellen et al. 2010; Sing et al. 2016; Tsiaras et al. 2016, 2018; Alonso-Floriano et al. 2019; Brogi & Line 2019; Sánchez-López et al. 2019; Cubillos et al. 2020; Santos et al. 2020; Giacobbe et al. 2021). In Sect. 2 we present our observations and data reduction process. In Sects. 3 and 4 we present the details of our chromatic Doppler tomography methodology and its implementation, describing the modeling and fitting procedures, respectively. In Sect. 5 the results of our analysis and a spectral retrieval on them are presented, along with the validation and examination of whether the result obtained by Santos et al. (2020) can be reproduced using the same ESPRESSO observations.We discuss and conclude our study in Sect. 6.

2. Observations and methodology

2.1. ESPRESSO observations

Two transits of HD 209458b were observed with ESPRESSO (Pepe et al. 2010, 2021), a fiber-fed spectrograph located at the Very Large Telescope (VLT) that covers a wavelength range from 380 to 788 nm at a resolution of $R \sim 140\,000$, on the nights of July 19, 2019, and September 10, 2019. The observations were acquired through the ESPRESSO consortium's guaranteed time observations under program 1102.C-0744 and had already been analyzed using different methodologies by Santos et al. (2020) and Casasayas-Barris et al. (2021). Both transits were observed using the UT3 telescope in the HR21 mode with the same exposure time of 175 s, which yielded a total of 89 and 85 exposures with an averaged signal-to-noise ratio (S/N) of 234 and 193 at 588 nm (physical order 104) for the two nights, respectively. It should be noted that the HR21 mode employs a slower readout that introduces a lower noise value per readout and reads two pixels in the spatial direction at once to reduce the number of readouts. The resulting spectra were reduced using the latest Data Reduction Software (DRS) pipeline, version 2.2.8. Each observed spectrum was divided into 85 echelle interference "orders". The DRS calculates and delivers the cross-correlation function (CCF) for each spectral order, as well as for the whole wavelength range. Based on the spectral type of the host star, HD 209458, the CCFs were generated using an F9V mask. We note that some orders are heavily contaminated by tellurics, and thus they are masked by the DRS and have no CCFs available. In this work we present the results obtained using the sky-subtracted (SKYSUB) data set. Nevertheless, we see no significant impact on the final results when using the SKYSUB or the non-SKYSUB products extracted by the DRS (see Appendix E). Additionally, due to the optical design of ESPRESSO and its image slicer, each order was repeated twice, and thus in practice we see a total of 170 "slices" (Pepe et al. 2021; Santos et al. 2020).

2.2. Data analysis

We processed our observations by applying the following procedure. The first step was the normalization of CCFs. The continuum levels of the CCFs are arbitrary because ESPRESSO

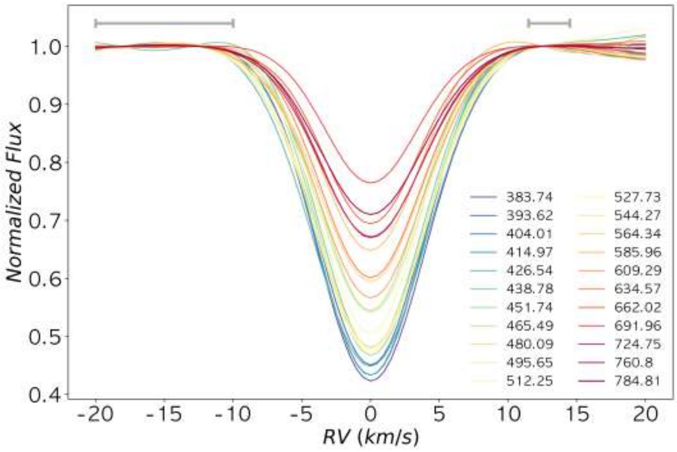

Fig. 1. Master CCF of each bin (central wavelength of each bin given in nm) from the Night 1 eight-slice-bin data sets. The solid gray lines mark the continuum regions of the CCFs that were used in the normalization.

observations are not flux-calibrated. For this reason, we needed to normalize each CCF by its continuum level. The normalization was done by fitting a second-order polynomial[1] to the continuum of each CCF. Specifically, we defined the continuum as regions with $-20 < v < -10$ km s^{-1} and $11 < v < 14$ km s^{-1} of each individual CCF in each slice (i.e., the continuum regions marked by the solid gray lines in Fig. 1). The continuum regions are defined asymmetrically to avoid some anomalies observed in the right side of the CCF continuum for certain slices[2]. Subsequently, we normalized each CCF by dividing them by the fitted polynomial.

The second step was the subtraction of the Keplerian motion of the star. The objective of this step was to remove the stellar RV that is induced by the planet while leaving the RM signal unaffected. Each CCF was shifted to the stellar rest frame via the introduction of an offset in its RV. This allowed the Keplerian motion of the star induced by its planet to be subtracted, leaving only the imprint in RV due to the rotation of the star (in addition to the instrumental broadening). The systemic velocity was removed as well. To perform this step, we used the *SinRadVel* function from the *PyAstronomy* python module (Czesla et al. 2019), which calculates and returns the RV shift according to the defined planetary and stellar parameters: orbital period, mid-transit time, stellar RV semi-amplitude, and the host star's systemic RV (see Table 1). Finally, all CCFs were linearly interpolated to the same RV grid (defined in the $-20 < v < 20$ km s^{-1} range with a step of 0.5 km s^{-1}) so that every CCF is evaluated at exactly the same RV values. The interpolation was required in order to subsequently perform mathematical operations between CCFs.

The third step was the definition of the wavelength bins. The CCFs were reassembled in eight-slice bins using the mean of the slices. The binning definition applied here is analogous to the one presented in Santos et al. (2020). The exact correspondence between the bins and the range of wavelengths covered by each bin is given in Table A.1. We note that there is a slight overlap in wavelength between adjacent bins as a consequence of the way orders are created by dispersion plus cross-dispersion, as seen on ESPRESSO and similar echelle spectrographs.

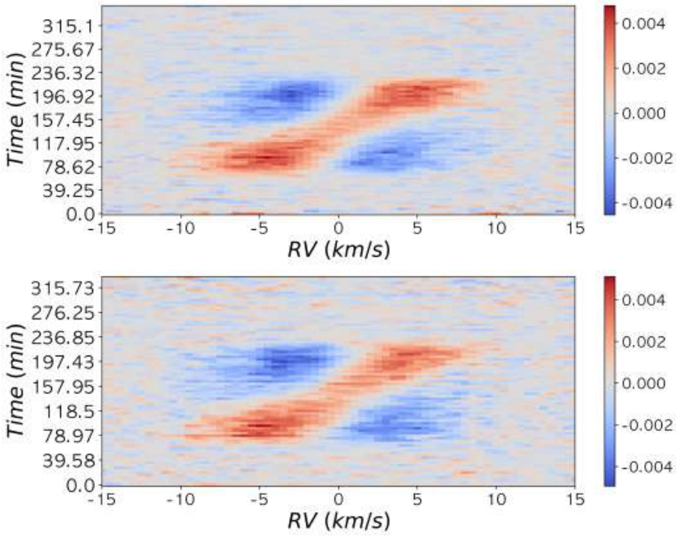

Fig. 2. CCF residual matrix using the 439-nanometer-centered bin from Night 1 (*top*) and Night 2 (*bottom*) after applying the steps from Sect. 2.2.

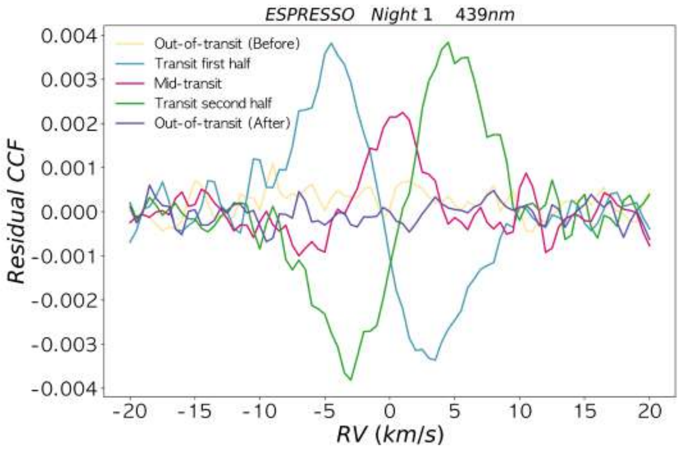

Fig. 3. Residual CCFs from the ESPRESSO Night 1 data set at the 439 nm bin. Two out-of-transit CCFs (before and after transit) and three in-transit CCFs (mid-transit and before and after mid-transit) are shown.

The fourth step was the generation of the master CCF. We calculated the average of all the out-of-transit CCFs (master CCFs hereafter) for each wavelength bin. The master CCF of each bin for Night 1 is presented in Fig. 1.

The fifth step was the subtraction of the master CCF: For each spectral bin, we subtracted its master CCF from the whole CCF times series. This subtraction yielded a chronological map of residual CCFs, showing the Doppler tomography anomalies expected during transit (see Fig. 2).

Following the application of the above steps to each data set, a chronological sequence of residual CCFs for each bin was obtained, what we refer to as the "CCF residual matrix". Figure 3 shows five residual CCFs (out-of-transit, in-transit, and mid-transit) for the 452-nanometer-centered bin of the ESPRESSO Night 1 data set to demonstrate the data reduction procedure. It is worth noting that each residual CCF in Fig. 3 corresponds to one row in the maps shown in Fig. 2. Finally, a Python function was

---

[1] We chose the second-order polynomial for CCF normalization after testing both first- and second-order choices and concluding that the second-order polynomial allowed for a more robust fitting to the continuum, allowing for better CCF normalization with less residuals in the continuum.

[2] These anomalies may be related to the humps caused by blended lines described in Lafarga et al. (2020).

developed to aggregate the data collected over different nights and compute the average of the residual CCF maps. We note that the observations were acquired using the same exposure time for both nights (175 s), so the number of samples in-transit are exactly the same for both nights. Thus, in practice we combined data points that have very similar in-transit phases.

The sixth and final step was error estimation. The noise of each data set in each wavelength bin was estimated with the standard deviation calculated at the RV regions in the CCF residual matrix that were far from the anomalies observed during the transit (regions marked as line-filled rectangles in Fig. B.1).

3. Model

To model our observed CCF residual matrix, we used the publicly available tool `SOAP3.0` (hereafter `SOAP`). This tool uses a pixelation approach to simulate a transiting planet in front of a rotating host star and delivers the overall photometric and RV measurements of the system (Boisse et al. 2012; Oshagh et al. 2013; Dumusque et al. 2014; Akinsanmi et al. 2018). Specifically, `SOAP` divides the star into a grid of $N \times N$ cells, each of which has its own Gaussian that is defined by the full width at half maximum (FWHM) σ_0 and depth parameters $prof_0$, which correspond to the non-rotating star's CCF. Subsequently, each cell's Gaussian is Doppler-shifted to account for stellar rotation, and its intensity is weighted using a quadratic limb-darkening law. Finally, the intensity in each cell is reduced to zero if the cell is blocked by the transiting planet. All of the cells are eventually summed up to obtain a single integrated CCF over the entire stellar disk. In order to have a model compatible with our observed CCF residual matrix, steps similar to the fourth and fifth steps in the data reduction procedure were carried out on the `SOAP` output CCFs. This led to a `SOAP` CCF residual matrix, which can be used to model the observations.

The coefficients of the quadratic stellar limb-darkening law (u_1 and u_2), which are the only wavelength-dependent `SOAP` parameters, are taken from the Limb Darkening Toolkit (`LDTk`) estimations (Parviainen & Aigrain 2015). `LDTk` provides an estimation of the quadratic limb-darkening coefficients for each wavelength bin based on the effective temperature ($T_{\rm eff}$ = 6118 ± 25 K), the surface gravity ($\log g$ = 4.36 ± 0.04), and the metallicity ([Fe/H] = 0.02 ± 0.05 dex) of the star (Sousa et al. 2008).

4. Fitting procedure

As previously mentioned, among all the fixed parameters in the `SOAP` models, the FWHM and depth values of the Gaussian-modeled CCF are especially relevant to performing a chromatic fitting to the data using `SOAP` models. For this reason, prior to the radius and limb-darkening coefficients fitting process (explained in Sect. 4.1), we needed to fit the `SOAP` CCF to the master CCF in each wavelength bin through a minimum χ^2 method (Fig. C.1) and obtain the FWHM and depth values of the Gaussian from the best fit. The resulting values for the FWHM and the depth of the Gaussian were fixed in `SOAP` configuration for each wavelength bin[3] before the `emcee`-based fitting procedure was executed to determine the $R_{\rm P}/R_*$, u_1, and u_2 posterior distributions. We are aware that the estimated values of $R_{\rm P}/R_*$ might be affected by the choice of $P_{\rm rot}$. However, since we are only interested in the relative changes in $R_{\rm P}/R_*$ as a function of wavelength, this arbitrary offset will not lead to any misinterpretation of the retrieved transmission spectra.

Table 1. Stellar, planetary, and simulation parameters fixed in the `SOAP` configuration to produce `SOAP` models.

Parameter	Unit	Value
Stellar parameters		
Radius (R_*) [a]	($R_\odot$)	1.203
Rotation period ($P_{\rm rot}$) [b]	(days)	15.7
Inclination angle (i) [c]	(°)	90
Effective temperature ($T_{\rm eff}$) [d]	(K)	6118
Planet parameters		
Orbital period ($P_{\rm orb}$) [e]	(days)	3.52472
Eccentricity (e) [f]		0.0082
Argument of periastron (ω)	(°)	90
Inclination of the planetary orbit ($i_{\rm p}$) [g]	(°)	86.59
Projected spin-orbit angle (λ) [h]	(°)	0.6
Semi-major axis (a) [c]	(R_*)	8.48509
`SOAP` simulation parameters		
Grid		300
Instrument resolution		100 000
RV step of CCF	(km s^{-1})	0.5
Width of CCF window	(km s^{-1})	25

References. [a] Boyajian et al. (2015), [b] Mazeh et al. (2000), [c] Southworth (2010), [d] Sousa et al. (2008), [e] Bonomo et al. (2017), [f] Wang & Ford (2011), [g] Winn et al. (2005), [h] Santos et al. (2020).

4.1. Radius and limb-darkening fitting

Our fitting procedure is based on fitting the observed chromatic CCF residual matrix with a synthetic CCF residual matrix generated with `SOAP`[4]. We used the planet radius and limb-darkening coefficients as our free parameters during the fitting process since they are the only wavelength-dependent parameters. The remaining required parameters in `SOAP` were adjusted to their values for HD 209458 and HD 209458b, which were taken from Mazeh et al. (2000), Winn et al. (2005), Southworth (2010), Wang & Ford (2011), Boyajian et al. (2015), Bonomo et al. (2017), and Santos et al. (2020) and are listed in Table 1. Since we are only interested in the relative changes in planet radius as a function of wavelength, fitting these fixed `SOAP` parameters is not necessary. Thus, we only fit $R_{\rm P}/R_*$, u_1, and u_2 through this procedure. This is a common approach for retrieving transmission spectra that is frequently used in the chromatic RM technique (Di Gloria et al. 2015; Oshagh et al. 2020; Santos et al. 2020).

Applying a Markov chain Monte Carlo (MCMC) approach, using the affine invariant ensemble sampler `emcee` package (Foreman-Mackey et al. 2013), the best-fit parameters and their associated uncertainties were calculated. The initial values for our free parameters were randomly initiated for ten MCMC chains inside the prior distributions. For each chain, we used a burn-in phase of 300 steps and then again sampled the chains for 1000 steps. Thus, the results concatenated to produce 10 000 steps. The best-fit values were estimated by

---

[3] These two parameters could be fit as extra free parameters through the `emcee` fitting procedure explained in Sect. 4.1. However, after testing this in several wavelength bins, we discarded the five-free-parameter fitting option because it implied a high computational cost without a significant contribution to the final results.

[4] We only considered in-transit regions of the CCF residual matrix in our fitting procedure.

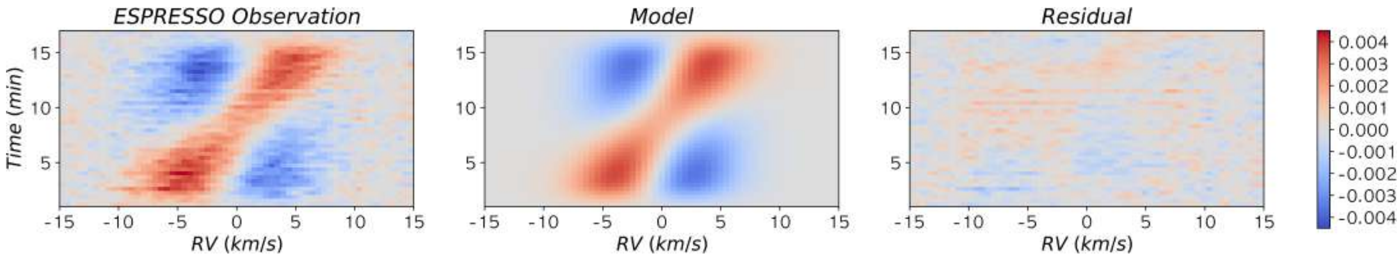

Fig. 4. Comparison between the observed CCF residual matrix for the 439-nanometer-centered bin (*left*), the best-fit `SOAP`-modeled CCF residual matrix (*center*), and the residuals of the fitting (*right*).

calculating the median values of the posterior distributions for each parameter.

Because the estimates of the limb-darkening coefficients were calculated using a stellar model, they may be inaccurate. It has been shown that incorrect values can induce biases in the retrieved transmission spectra in multiband photometry (e.g., Csizmadia et al. 2013; Espinoza & Jordán 2015; Espinoza & Jordán 2016; Morello et al. 2017; Morello 2018). Thus, we left the u_1 and u_2 coefficients free during the fitting procedure[5].

We imposed a very wide and uninformative uniform prior on the planet radius, $0.1 < R_P/R_* < 0.2$, which is 100 times wider than the prior imposed by Santos et al. (2020). The priors on the limb-darkening coefficients were constrained by Gaussian priors created using `LDTk` (Parviainen & Aigrain 2015) for all the wavelength bins (i.e., $\mathcal{N}(\mu_{\mathrm{LDTk}}; 0.05)$[6]). We note that 0.05 corresponds to three times the limb-darkening coefficients errors estimated by `LDTk`.

To illustrate the performance of our fitting procedure, we show in Fig. 4 a comparison between an observed CCF residual matrix, its best-fit `SOAP`-modeled CCF residual matrix, and the residuals between the best-fit model and observations. This `emcee`-based fitting approach allows the posterior distributions of the planet-to-star radius ratio and the limb-darkening coefficients to be obtained (Fig. D.1) at every defined wavelength bin. In this way, we determined the values of these parameters and their uncertainties as the most probable value and the 1σ error in each posterior distribution.

5. Results

5.1. The CHOCOLATE transmission spectrum

The transmission spectrum of HD 209458b, resulting from our fit to 21 wavelength bins and combining the SKYSUB data from two nights, is shown in Fig. 5 (see values in Table A.1). The non-SKYSUB data results are given in Fig. E.1. The retrieved transmission spectra from individual transits agree well with one another and with the combined nights (Fig. F.1). Our data are the same as used in Santos et al. (2020), although they employed the chromatic RM method on the combined two nights to retrieve the broadband transmission spectra of HD 209458b. Figure 5 shows a comparison of our results with those presented in Santos et al. (2020) and with the transmission spectrum obtained from STIS multiband photometry data from the *Hubble* Space Telescope (HST; Sing et al. 2016).

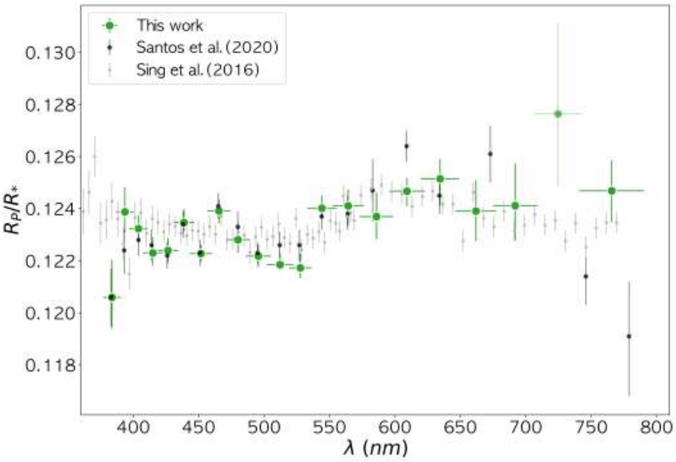

Fig. 5. Comparison between the transmission spectra of HD 209458b obtained by Santos et al. (2020) (black circle), by Sing et al. (2016) (gray circle), and from our analysis (green circle). The x-axis error bars stand for the width of the wavelength bin, while the y-axis error bars stand for the uncertainties of the estimated planet-star radius ratio in each wavelength bin taken as the 1σ values of the posterior distributions from the fitting. We applied an offset to the values of the radius ratio obtained from our analysis, subtracting the average difference between our values and the Santos et al. (2020) values. Similarly, we introduced an offset to the Sing et al. (2016) data set to subtract the average difference with the Santos et al. (2020) values.

Our retrieved transmission spectrum agrees well with both the Santos et al. (2020) and Sing et al. (2016) results. Moreover, the achieved precision on the planet radius in each wavelength bin combining two transits is compatible with the ones obtained from HST and ESPRESSO. In particular, the comparison between the transmission spectrum obtained through our analysis and the spectrum presented by Santos et al. (2020) reveals identical patterns. We find a mostly flat spectrum with a strong increase in radius above 550 nm, which is consistent with both comparison spectra. Our study, however, shows less scatter than Santos et al. (2020), especially above 550 nm, where the retrieved spectrum is more in line with Sing et al. (2016).

Two spectral bins, centered at 384 and 725 nm, deviate noticeably from the general trend of the spectrum. The 384 nm bin contains the spectral slices from the bluest edge of the ESPRESSO and has a low S/N. The retrieved transmission spectrum by Santos et al. (2020) exhibits a similar deviation in this first bin. Regarding the 725 nm bin, we identify a notable deviation compared to the Sing et al. (2016) spectrum, which is probably caused by the strong telluric contamination by H_2O and O_2 in the last two bins of our spectra (Smette et al. 2015). Santos et al. (2020) were not able to obtain transmission data in this bin.

---

[5] Our estimated limb-darkening coefficients values are close to the LDTk values; therefore, fixing the limb-darkening coefficients would not influence the retrieved transmission spectrum.

[6] $\mathcal{U}(a; b)$ is a uniform prior with lower and upper limits of a and b. $\mathcal{N}(\mu; \sigma)$ is a normal distribution with mean μ and width σ.

Table 2. Bayesian evidence for various model assumptions obtained from three versions of the transmission spectrum.

#	Model assumption	Full w/ offset		Full w/o offset		w/o 725 nm & w/ offset	
		$\ln\mathcal{Z}$	$\Delta\ln\mathcal{Z}$	$\ln\mathcal{Z}$	$\Delta\ln\mathcal{Z}$	$\ln\mathcal{Z}$	$\Delta\ln\mathcal{Z}$
	Planetary atmosphere (uniform clouds)						
1	No additional absorbers	125.63	ref.	124.90	ref.	120.75	ref.
2	Na	129.82	4.2	129.02	4.1	125.07	4.3
3	K	128.95	3.3	127.85	2.9	123.37	2.6
4	TiO	129.03	3.4	128.18	3.3	123.96	3.2
5	VO	127.14	1.5	126.57	1.7	122.09	1.3
6	H_2O	129.82	4.2	129.33	4.4	123.77	3.0
7	NH_3	133.28	7.7	132.58	7.7	127.44	6.7
8	NH_3+Na	132.77	7.1	132.02	7.1	127.15	6.4
9	NH_3+K	132.87	7.2	132.13	7.2	126.95	6.2
10	NH_3+TiO	129.79	4.2	128.83	3.9	124.60	3.8
11	NH_3+VO	129.27	3.6	128.76	3.9	123.84	3.1
12	NH_3+H_2O	133.44	7.8	132.61	7.7	127.36	6.6
13	NH_3+H_2O+Na+K	132.65	7.0	131.91	7.0	126.94	6.2
14	NH_3+H_2O+Na+K+TiO+VO	129.11	3.5	128.91	3.4	123.79	3.0
15	Na+TiO	129.23	3.6	128.38	3.5	124.27	3.5
	Stellar contamination						
16	Spots+Faculae	126.57	0.9	125.92	1.0	121.28	0.5
	Planetary atmosphere (uniform clouds) and stellar contamination combined						
17	NH_3+H_2O+Spots+Faculae	130.97	5.3	130.50	5.6	124.69	3.9
	Planetary atmosphere (patchy clouds)						
18	NH_3	129.29	3.7	128.85	4.0	123.80	3.1
19	NH_3+H_2O	129.59	4.0	129.37	4.5	123.73	3.0
	Planetary atmosphere (patchy clouds) and stellar contamination combined						
20	NH_3+H_2O+Spots+Faculae	128.91	3.3	128.94	4.0	123.23	2.5

5.2. Atmospheric retrieval

We performed spectral retrieval analyses on the ESPRESSO transmission spectrum (21 wavelength bins). The model consists of two components:

$$D_{\lambda,\rm obs} = D_{\lambda,\rm true} \times \epsilon_\lambda, \tag{1}$$

where $D_{\lambda,\rm true}$ comes from the planetary atmosphere and ϵ_λ refers to the stellar contamination.

The forward model of the planetary atmosphere was implemented by PLATON (PLanetary Atmospheric Transmission for Observer Noobs; Zhang et al. 2019, 2020), which is parameterized by: the planet radius at 1 bar ($R_{\rm p,1bar}$), an isothermal temperature ($T_{\rm iso}$), the cloud-top pressure ($P_{\rm cloud}$) for the assumption of uniform clouds, an enhancement factor over the nominal H_2 Rayleigh scattering ($A_{\rm RS}$), and the volume mixing ratio for a given species other than H, H_2, and He (X_i). The atmosphere was assumed to be dominated by hydrogen and helium, with a solar composition of H, H_2, and He. Fixed values were adopted in the forward model for the planet mass ($M_{\rm p}$ = 0.714 $M_{\rm J}$) and the stellar radius (R_* = 1.162 $R_\odot$) from TEPCat (Transiting Extrasolar Planets CATalogue, Southworth 2011).

The stellar contamination (McCullough et al. 2014; Rackham et al. 2018, 2019) included the contribution from both spots and faculae, which is parameterized by the spot temperature ($T_{\rm spot}$), the spot coverage ($f_{\rm spot}$), the facula temperature ($T_{\rm facu}$), and the facula coverage ($f_{\rm facu}$), in the form of

$$\epsilon_\lambda = \frac{1}{1 - f_{\rm spot}\left(1 - \frac{S_{\lambda,T_{\rm spot}}}{S_{\lambda,T_{\rm phot}}}\right) - f_{\rm facu}\left(1 - \frac{S_{\lambda,T_{\rm facu}}}{S_{\lambda,T_{\rm phot}}}\right)}, \tag{2}$$

where the spectrum $S_{\lambda,T}$ was interpolated in the BT-NextGen (AGSS2009) stellar spectral grid (Allard et al. 2012) provided in PLATON. The photosphere was assumed to have a temperature of $T_{\rm phot}$ = 6118 K.

To explain the ESPRESSO transmission spectrum, we considered three scenarios: (I) a purely planetary atmosphere (i.e., $\epsilon_\lambda = 1$), (II) a purely stellar contamination (i.e., $D_{\lambda,\rm true} = D_0$), and (III) a combination of both planetary atmosphere and stellar contamination. We used `PyMultiNest` (Buchner et al. 2014) to implement the multimodal nested sampling to explore the posteriors, which also gives the Bayesian evidence ($\mathcal{Z}$). A total of 1000 live points were adopted in each retrieval analysis, resulting in a typical uncertainty of ~0.07–0.10 for $\ln\mathcal{Z}$. Table 2 summarizes the resulting $\ln\mathcal{Z}$ of various model assumptions. Figure 6 shows a selection of those listed in Table 2. Table 3 presents the representative prior setup and posterior estimates for scenario III. The criteria of Kass & Raftery (1995) were adopted to interpret the Bayes factor ($B_{10} = \mathcal{Z}_1/\mathcal{Z}_0$) of two hypotheses, where $\Delta\ln\mathcal{Z} = 1, 3, 5$ are considered as the starting points of positive, strong, and very strong, respectively.

In the scenario of a purely planetary atmosphere, the model assumption of no additional absorbers other than H, H_2, and

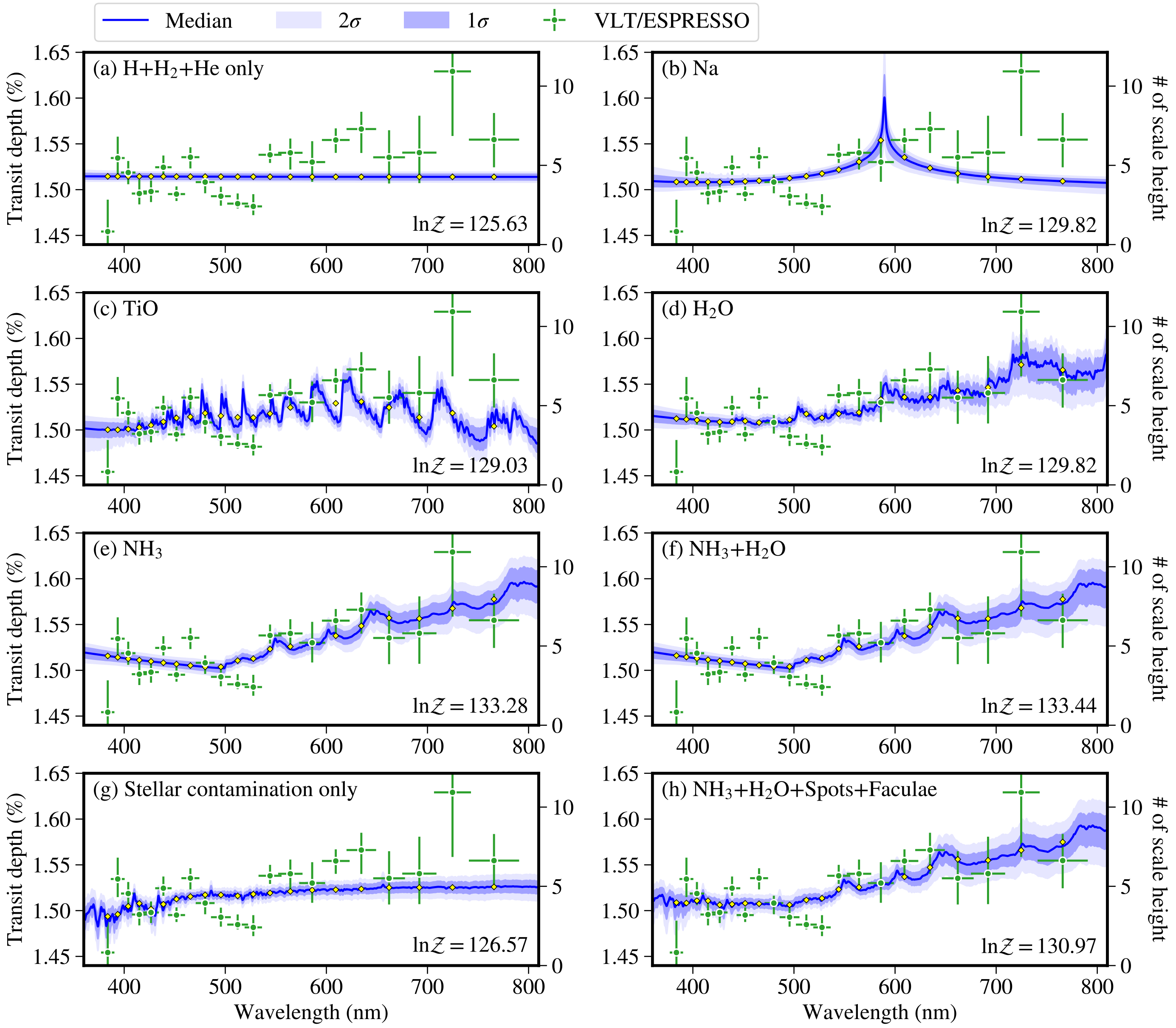

Fig. 6. Comparison between the ESPRESSO transmission spectrum and the retrieval analyses under different model assumptions. *Panel a* considers a planetary atmosphere composed of only H, H_2, and He. Additional gas absorbers are added in *Panels b–f*. *Panel g* assumes only the stellar contamination to account for any transit depth variation, while *Panel h* includes both planetary atmosphere and stellar contamination. Of these model assumptions, an atmosphere containing H_2O and NH_3 gives the highest Bayesian evidence (*Panel f*).

He is considered as a reference since it could be a flat line or a Rayleigh scattering slope, depending on the altitude of the cloud deck. To the base of H, H_2, and He, a variety of additional optical absorbers, including Na, K, TiO, VO, H_2O, and NH_3, were then added to the atmosphere to explore the contribution of the observed spectral signature. The models with additional optical absorbers are always strongly favored over the reference model, except for VO at a positive level. The most favored model assumption is the model with NH_3 or with both NH_3 and H_2O. In contrast, the ESPRESSO transmission spectrum cannot be explained by the scenario of purely stellar contamination. Finally, we investigated the scenario of a combination of both planetary atmosphere and stellar contamination, where the component of planetary atmosphere included additional absorbers of both NH_3 and H_2O. This model assumption (Model 17) decreases the Bayesian evidence by $\Delta \ln \mathcal{Z} = 2.5$ compared to the scenario of a purely planetary atmosphere (Model 12), indicating that the data are positively against the inclusion of stellar contamination in the model assumption. Nevertheless, the inclusion of stellar contamination barely changes the retrieved atmospheric parameters (see Fig. 7).

Furthermore, we performed the same retrieval analyses on the transmission spectrum without subtracting an offset of 0.005 and on the transmission spectrum without the 725 nm bin. In both cases, the model selection results remain the same, that is, the models with NH_3 are always favored by our data. The resulting posteriors also remain consistent for all the parameters except for $R_{\rm p,1bar}$, which would be larger if the offset were not subtracted. In addition to the assumption of uniform clouds, we also experimented with the assumption of patchy clouds with an additional free parameter to account for the cloud coverage. However, the assumption of patchy clouds is strongly disfavored by our

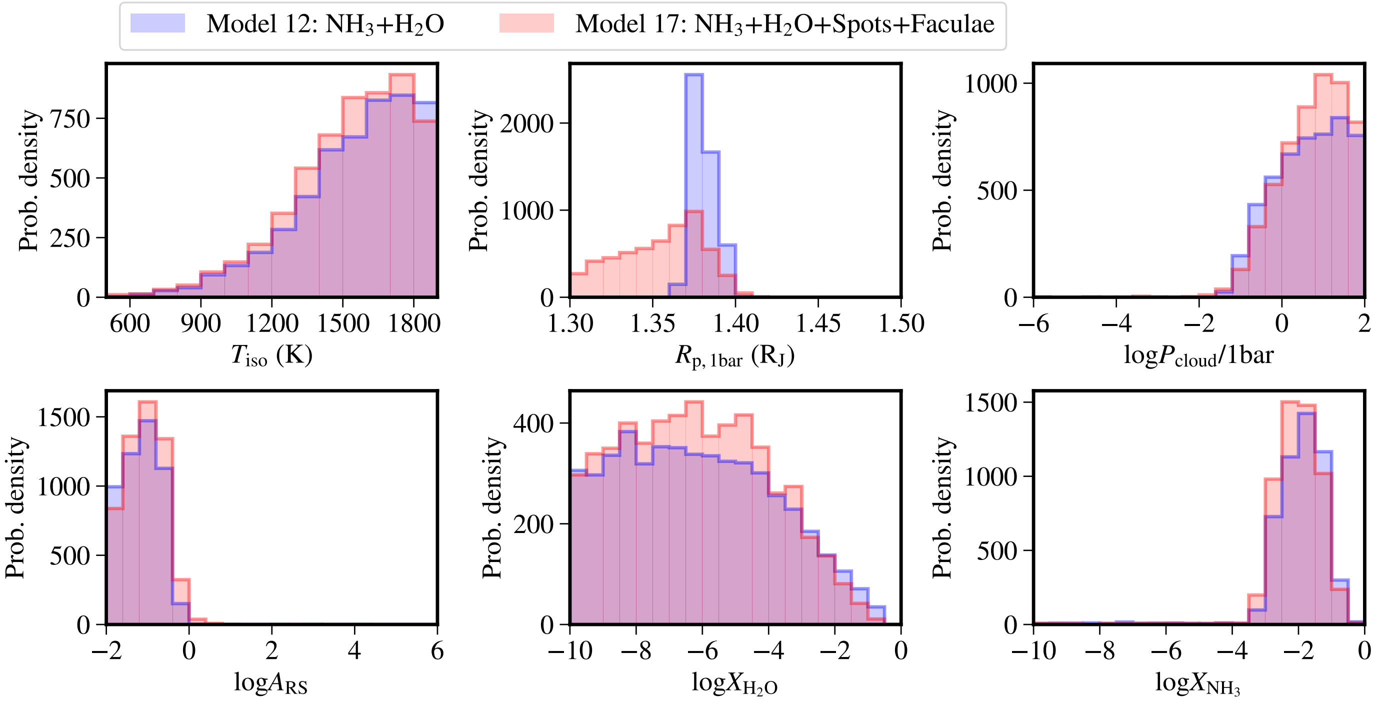

Fig. 7. Posterior distributions of the common atmospheric parameters in Model 12 and Model 17.

Table 3. Parameter priors and posteriors for the spectral retrievals.

Parameter	Prior	Posterior
	Planetary atmosphere	
$R_{\rm p,1bar}$ ($R_{\rm J}$)	$\mathcal{U}(1.3, 1.5)$	$1.36^{+0.021}_{-0.034}$
$T_{\rm iso}$ (K)	$\mathcal{U}(500, 1900)$	1576^{+207}_{-293}
$\log P_{\rm cloud}/1{\rm bar}$	$\mathcal{U}(-6, 2)$	$0.8^{+0.7}_{-0.9}$
$\log A_{\rm RS}$	$\mathcal{U}(-2, 6)$	$-1.1^{+0.5}_{-0.5}$
$\log X_{\rm H_2O}$	$\mathcal{U}(-10, 0)$	$-6.3^{+2.5}_{-2.4}$
$\log X_{\rm NH_3}$	$\mathcal{U}(-10, 0)$	$-2.0^{+0.7}_{-0.7}$
	Stellar contamination	
$T_{\rm spot}$ (K)	$\mathcal{U}(2000, 5918)$	3312^{+1365}_{-806}
$f_{\rm spot}$ (%)	$\mathcal{U}(0, 100)$	5^{+5}_{-3}
$T_{\rm facu}$ (K)	$\mathcal{U}(6118, 7000)$	6193^{+122}_{-55}
$f_{\rm facu}$ (%)	$\mathcal{U}(0, 100)$	14^{+25}_{-10}

Notes. In the spectral retrieval analyses, the model assumption could be a purely planetary atmosphere, purely stellar contamination, or a combination of the two. The table presents the posterior estimates for the model assumption in which both planetary atmosphere (with NH$_3$ and H$_2$O) and stellar contamination are considered, i.e., Model 17 in Table 2.

data according to the decreasing model evidence, as shown in Table 2.

Santos et al. (2020) found that Na, TiO, or both were favored by their version of the ESPRESSO transmission spectrum. By investigating more optical absorbers, our retrieval analyses indicate that NH$_3$ is likely present in the atmosphere of HD 209458b. On the other hand, in the presence of NH$_3$, it is not possible to distinguish whether or not Na, K, or H$_2$O exists, while TiO and VO are strongly disfavored.

Our potential inference of NH$_3$ is consistent with recent studies on the same planet. MacDonald & Madhusudhan (2017) reported the first possible inference of NH$_3$ using the low-resolution transmission spectrum acquired with the Wide Field Camera 3 (WFC3) aboard the HST. Using the high-resolution cross-correlation technique, Giacobbe et al. (2021) robustly detected NH$_3$ in the transmission spectrum; H$_2$O, CO, HCN, CH$_4$, and C$_2$H$_2$ were also detected with the near-infrared echelle spectrograph GIANO-B mounted at the 3.6 m Telescopio Nazionale *Galileo*.

Recently, Casasayas-Barris et al. (2021) explored the atmosphere of HD 209458b, also using these same ESPRESSO observations. They did not detect Na absorption in the high-resolution transmission spectrum of this planet around single lines, due to the overlap of the Doppler shadow and the position of the expected atmospheric absorption. Our best model is not conclusive regarding the presence of Na.

6. Discussion and conclusions

In this work we have developed a novel chromatic line-profile tomography technique, named CHOCOLATE, to retrieve the broadband transmission spectrum of transiting exoplanets using high-resolution spectroscopy. The CHOCOLATE method utilizes the `SOAP` code to produce physically motivated Doppler tomography models in different wavelength bins; it then uses these `SOAP` models to fit the observational data via an MCMC fitting procedure. We validated its performance on an ESPRESSO data set of the well-known and well-studied exoplanet HD 209458b.

The transmission spectrum of HD 209458b obtained through CHOCOLATE agrees extremely well with previous results (Santos et al. 2020; Sing et al. 2016) that were derived using different methods and data, thus demonstrating its usefulness and reliability. We have shown that our methodology achieves similar precision (even better in some bins) as the different methodologies (i.e., chromatic RM) using the same data (Santos et al. 2020). We have explored different scenarios using PLATON and found that a planetary atmosphere model containing H_2O and NH_3 is the preferred scenario, as derived from the spectral retrieval on the transmission spectrum, with a confidence of $\Delta \ln \mathcal{Z} = 7.8$.

In our study we use a version of SOAP that assumes CCFs to be pure Gaussian, while in reality stellar CCFs have a so-called C shape due to the stellar granulation (Dravins et al. 1981; Dumusque et al. 2014). Additionally, removing or masking strong spectral lines known to be affected by short-term variability in the ESPRESSO 1D spectra could further improve the stability of the CCFs, especially on the redder orders. Probing the impact of these differences is beyond scope of the current paper but will be pursued in forthcoming works.

The application of the CHOCOLATE methodology is especially interesting for future studies on exoplanets around moderate and fast rotating stars, where the chromatic RM method cannot be applied due to the fact that the RV precision is dominated by the rotational broadening of the star. Moreover, for planets around young and very active host stars, where the CCF residual matrix is heavily affected by the presence of stellar active regions (Palle et al. 2020), CHOCOLATE could assist by more efficiently modeling and retrieving their transmission spectra, taking `SOAP`'s ability to model stellar active regions into account.

There has been a recent discussion in the literature about the great potential of simultaneously exploring exoplanet atmospheres at low and high spectral resolution (Brogi et al. 2017; Pino et al. 2018). This is because high-resolution transmission spectroscopy probes the cores of spectral lines generated in the planetary thermosphere and exosphere, including those of escaping material, while low-resolution spectroscopy is more sensitive to the higher planetary troposphere and can capture broader spectral features, such as molecular bands, clouds and hazes, or Rayleigh scattering processes. Our results demonstrate how it will be possible, using only high dispersion spectroscopy, to retrieve the broad transmission spectrum of a planet, which had previously been thought to only be possible via low-resolution observations. This will be particularly important in the era of extremely large telescopes (ELTs). Given their small field of view and a general lack of suitable comparison stars, low-resolution spectroscopy will generally not be possible. High-resolution spectroscopy with fiber-fed ultra-stable spectrographs, via the use of CHOCOLATE and similar techniques, will be able to probe both the lines profiles and the broad continuum features of exoplanet transmission spectra, providing a complete picture of their atmospheres.

Acknowledgements. We thank the anonymous referee for insightful suggestions, which added the clarity of this paper. E.E.-B. acknowledges financial support from the European Union and the State Agency of Investigation of the Spanish Ministry of Science and Innovation (MICINN) under the grant PRE2020-093107 of the Pre-Doc Program for the Training of Doctors (FPI-SO) through FEDER, FSE and FDCAN funds. E.E.-B. also wants to acknowledge funding from the Instituto de Astrofísica de Canarias (IAC) Summer Grant in Astrophysics 2020. This work is partly financed by the Spanish Ministry of Economics and Competitiveness through grants PGC2018-098153-B-C31. The ESPRESSO Instrument Project was partially funded through SNSF's FLARE Programme for large infrastructures. This work made use of PyAstronomy. G.C. acknowledges the support by the National Natural Science Foundation of China (Grant No. 42075122, 12122308), the Natural Science Foundation of Jiangsu Province (Grant No. BK20190110), and Youth Innovation Promotion Association CAS (2021315). This work was supported by FCT – Fundação para a Ciência e a Tecnologia through national funds and by FEDER through COMPETE2020 – Programa Operacional Competitividade e Internacionalização by these grants: UID/FIS/04434/2019; UIDB/04434/2020; UIDP/04434/2020; PTDC/FIS-AST/32113/2017 & POCI-01-0145-FEDER-032113; PTDC/FIS-AST/28953/2017 & POCI-01-0145-FEDER-028953; PTDC/FIS-AST/28987/2017 & POCI-01-0145-FEDER-028987. This work has been carried out within the framework of the National Centre of Competence in Research PlanetS supported by the Swiss National Science Foundation. This project has received funding from the European Research Council (ERC) under the European Union's Horizon 2020 research and innovation programme (project Four Aces grant agreement No 724427). We acknowledge funding from the European Research Council under the European Union's Horizon 2020 research and innovation program under grant agreement No 694513. G.M. has received funding from the European Union's Horizon 2020 research and innovation programme under the Marie Skłodowska-Curie grant agreement No. 895525. R.A. is a Trottier Postdoctoral Fellow and acknowledges support from the Trottier Family Foundation. This work was supported in part through a grant from FRQNT. This work has been carried out within the framework of the National Centre of Competence in Research PlanetS supported by the Swiss National Science Foundation. The authors acknowledge the financial support of the SNSF. This work has been carried out in the frame of the National Centre for Competence in Research "PlanetS" supported by the Swiss National Science Foundation (SNSF). This project has received funding from the European Research Council (ERC) under the European Union's Horizon 2020 research and innovation programme (project SPICE DUNE, grant agreement No 947634). J.L.-B. acknowledges financial support received from "la Caixa" Foundation (ID 100010434) and from the European Union's Horizon 2020 research and innovation programme under the Marie Skłodowska-Curie grant agreement No 847648, with fellowship code LCF/BQ/PI20/11760023. O.D.S.D. is supported in the form of work contract (DL 57/2016/CP1364/CT0004) funded by national funds through Fundação para a Ciência e Tecnologia (FCT). V.A. acknowledges the support from FCT through Investigador FCT contract nr. IF/00650/2015/CP1273/CT0001. A.S.M. acknowledges financial support from the Spanish Ministry of Science and Innovation (MICINN) under the 2019 Juan de la Cierva Programme. A.S.M., J.I.G.H., C.A.P. and R.R. acknowledge financial support from the Spanish Ministry of Science and Innovation (MICINN) through projects AYA2017-86389-P. J.I.G.H. also acknowledges financial support from the Spanish MICINN under 2013 Ramón y Cajal program RYC-2013-14875. M.R.Z.O. acknowledges financial support through project PID2019-109522G8-C51. The INAF authors acknowledge financial support of the Italian Ministry of Education, University, and Research with PRIN 201278X4FL and the "Progetti Premiali" funding scheme.

References

Akinsanmi, B., Oshagh, M., Santos, N. C., & Barros, S. C. C. 2018, A&A, 609, A21
Allard, F., Homeier, D., & Freytag, B. 2012, Phil. Trans. R. Soc. London Ser. A, 370, 2765
Alonso-Floriano, F. J., Snellen, I. A. G., Czesla, S., et al. 2019, A&A, 629, A110
Boisse, I., Bonfils, X., & Santos, N. C. 2012, A&A, 545, A109
Bonomo, A. S., Desidera, S., Benatti, S., et al. 2017, A&A, 602, A107
Borsa, F., Rainer, M., & Poretti, E. 2016, A&A, 590, A84
Boyajian, T., von Braun, K., Feiden, G. A., et al. 2015, MNRAS, 447, 846
Brogi, M., & Line, M. R. 2019, AJ, 157, 114
Brogi, M., Line, M., Bean, J., Désert, J. M., & Schwarz, H. 2017, ApJ, 839, L2
Buchner, J., Georgakakis, A., Nandra, K., et al. 2014, A&A, 564, A125
Casasayas-Barris, N., Palle, E., Stangret, M., et al. 2021, A&A, 647, A26
Cegla, H. M., Lovis, C., Bourrier, V., Watson, C. A., & Wyttenbach, A. 2017, A&A, 598, L3
Charbonneau, D., Brown, T. M., Latham, D. W., & Mayor, M. 2000, ApJ, 529, L45
Charbonneau, D., Brown, T. M., Noyes, R. W., & Gilliland, R. L. 2002, ApJ, 568, 377
Collier Cameron, A., Bruce, V. A., Miller, G. R. M., Triaud, A. H. M. J., & Queloz, D. 2010, MNRAS, 403, 151
Csizmadia, S., Pasternacki, T., Dreyer, C., et al. 2013, A&A, 549, A9
Cubillos, P. E., Fossati, L., Koskinen, T., et al. 2020, AJ, 159, 111
Czesla, S., Schröter, S., Schneider, C. P., et al. 2019, PyA: Python astronomy-related packages, Astrophysics Source Code Library [`record ascl:1906.010`]
Di Gloria, E., Snellen, I. A. G., & Albrecht, S. 2015, A&A, 580, A84
Dravins, D., Lindegren, L., & Nordlund, A. 1981, A&A, 96, 345
Dumusque, X., Boisse, I., & Santos, N. C. 2014, ApJ, 796, 132
Espinoza, N., & Jordán, A. 2015, MNRAS, 450, 1879
Espinoza, N., & Jordán, A. 2016, MNRAS, 457, 3573
Foreman-Mackey, D., Hogg, D. W., Lang, D., & Goodman, J. 2013, PASP, 125, 306
Giacobbe, P., Brogi, M., Gandhi, S., et al. 2021, Nature, 592, 205
Hartman, J. D., Bakos, G. Á., Buchhave, L. A., et al. 2015, AJ, 150, 197

Henry, G. W., Marcy, G. W., Butler, R. P., & Vogt, S. S. 2000, ApJ, 529, L41

Holt, J. R. 1893, A&A, 12, 646

Johnson, M. C., Cochran, W. D., Collier Cameron, A., & Bayliss, D. 2015, ApJ, 810, L23

Kass, R. E., & Raftery, A. E. 1995, J. Am. Stat. Assoc., 90, 773

Lafarga, M., Ribas, I., Lovis, C., et al. 2020, A&A, 636, A36

MacDonald, R. J., & Madhusudhan, N. 2017, MNRAS, 469, 1979

Mazeh, T., Naef, D., Torres, G., et al. 2000, ApJ, 532, L55

McCullough, P. R., Crouzet, N., Deming, D., & Madhusudhan, N. 2014, ApJ, 791, 55

McLaughlin, D. B. 1924, ApJ, 60, 22

Morello, G. 2018, AJ, 156, 175

Morello, G., Tsiaras, A., Howarth, I. D., & Homeier, D. 2017, AJ, 154, 111

Oshagh, M., Boisse, I., Boué, G., et al. 2013, A&A, 549, A35

Oshagh, M., Bauer, F. F., Lafarga, M., et al. 2020, A&A, 643, A64

Palle, E., Oshagh, M., Casasayas-Barris, N., et al. 2020, A&A, 643, A25

Parviainen, H., & Aigrain, S. 2015, MNRAS, 453, 3821

Pepe, F. A., Cristiani, S., Rebolo Lopez, R., et al. 2010, Proc. SPIE, 7735, 77350F

Pepe, F., Cristiani, S., Rebolo, R., et al. 2021, A&A, 645, A96

Pino, L., Ehrenreich, D., Wyttenbach, A., et al. 2018, A&A, 612, A53

Rackham, B. V., Apai, D., & Giampapa, M. S. 2018, ApJ, 853, 122

Rackham, B. V., Apai, D., & Giampapa, M. S. 2019, AJ, 157, 96

Rossiter, R. A. 1924, ApJ, 60, 15

Sánchez-López, A., Alonso-Floriano, F. J., López-Puertas, M., et al. 2019, A&A, 630, A53

Santos, N. C., Cristo, E., Demangeon, O., et al. 2020, A&A, 644, A51

Sing, D. K., Fortney, J. J., Nikolov, N., et al. 2016, Nature, 529, 59

Smette, A., Sana, H., Noll, S., et al. 2015, A&A, 576, A77

Snellen, I. A. G. 2004, MNRAS, 353, L1

Snellen, I. A. G., de Kok, R. J., de Mooij, E. J. W., & Albrecht, S. 2010, Nature, 465, 1049

Sousa, S. G., Santos, N. C., Mayor, M., et al. 2008, A&A, 487, 373

Southworth, J. 2010, MNRAS, 408, 1689

Southworth, J. 2011, MNRAS, 417, 2166

Triaud, A. H. M. J. 2018, Handbook of Exoplanets, The Rossiter-McLaughlin Effect in Exoplanet Research, eds. H. J. Deeg, & J. A. Belmonte (Berlin: Springer), 2

Tsiaras, A., Waldmann, I. P., Rocchetto, M., et al. 2016, ApJ, 832, 202

Tsiaras, A., Waldmann, I. P., Zingales, T., et al. 2018, AJ, 155, 156

Wang, J., & Ford, E. B. 2011, MNRAS, 418, 1822

Winn, J. N., Noyes, R. W., Holman, M. J., et al. 2005, ApJ, 631, 1215

Zhang, M., Chachan, Y., Kempton, E. M. R., & Knutson, H. A. 2019, PASP, 131, 034501

Zhang, M., Chachan, Y., Kempton, E. M. R., Knutson, H. A., & Chang, W. H. 2020, ApJ, 899, 27

Zhou, G., Bakos, G. Á., Hartman, J. D., et al. 2017, AJ, 153, 211

Appendix A: Wavelength bin definition and numeric results

We specify in Table A.1 the exact correspondence between the defined bins and the range of wavelengths covered by each bin, which comes as an outcome of *Step 2* in the data reduction (Sect. 2.2). We also show in Table A.1 the estimated values for the radius and the limb-darkening coefficients from the fitting procedure.

Table A.1. Central wavelength, wavelength range covered by each defined bin, and planet-star radius ratio (R_P/R_*) values estimated through the fitting procedure for each wavelength bin using the SKYSUB data set (shown in Fig. 5). We note that a − 0.005 offset has been introduced to the resulting R_P/R_* values to subtract the average difference with the Santos et al. (2020) values. Each bin contains eight ESPRESSO slices, except the last one, which contains ten. Moreover, it should be noted that this wavelength binning definition does not involve spectral slice overlap, but a slight overlap in wavelength is present between adjacent bins as a consequence of the way orders are created by dispersion plus cross-dispersion, as seen on ESPRESSO and similar echelle spectrographs.

Bin	*Central Wavelength (nm)*	*Wavelength Range (nm)*	R_P/R_*
1	383.75	377.15 - 390.34	$0.1206^{+0.0014}_{-0.0012}$
2	393.62	386.76 - 400.48	$0.1239^{+0.0009}_{-0.0008}$
3	404.01	396.87 - 411.15	$0.1232^{+0.0005}_{-0.0005}$
4	414.98	407.53 - 422.42	$0.1223^{+0.0006}_{-0.0005}$
5	426.55	418.78 - 434.31	$0.1224^{+0.0005}_{-0.0005}$
6	438.78	430.67 - 446.89	$0.1235^{+0.0005}_{-0.0003}$
7	451.74	443.26 - 460.22	$0.1223^{+0.0003}_{-0.0003}$
8	465.49	456.60 - 474.38	$0.1239^{+0.0004}_{-0.0005}$
9	480.10	470.77 - 489.42	$0.1228^{+0.0003}_{-0.0005}$
10	495.65	485.85 - 505.45	$0.1222^{+0.0004}_{-0.0004}$
11	512.26	501.94 - 522.57	$0.1219^{+0.0005}_{-0.0002}$
12	527.73	519.13 - 536.33	$0.1217^{+0.0005}_{-0.0004}$
13	544.27	532.89 - 555.65	$0.1240^{+0.0005}_{-0.0004}$
14	564.35	552.27 - 576.42	$0.1241^{+0.0006}_{-0.0007}$
15	585.96	573.12 - 598.80	$0.1237^{+0.0009}_{-0.0009}$
16	609.30	595.60 - 622.99	$0.1247^{+0.0005}_{-0.0006}$
17	634.57	619.92 - 649.22	$0.1251^{+0.0008}_{-0.0010}$
18	662.03	646.31 - 677.74	$0.1239^{+0.0012}_{-0.0012}$
19	691.97	675.04 - 708.89	$0.1241^{+0.0016}_{-0.0013}$
20	724.75	706.46 - 743.04	$0.1276^{+0.0035}_{-0.0028}$
21	765.80	740.95 - 790.64	$0.1247^{+0.0012}_{-0.0012}$

Appendix B: Noise estimation

We show in Fig. B.1 the CCF residual matrix regions used to calculate the standard deviation for the noise estimation.

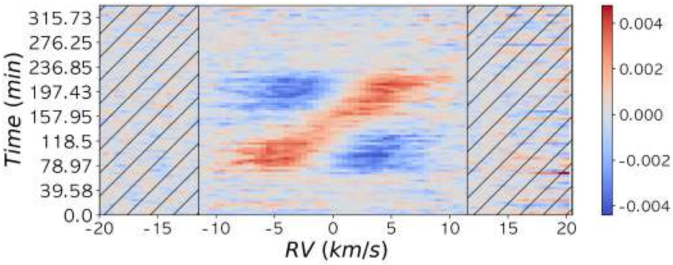

Fig. B.1. Regions used for the noise estimation (line-filled rectangles) marked over the processed data matrix using the 426-nanometer-centered bin as an example.

Appendix C: `SOAP` CCF fitting

In this appendix we show the procedure used to fit `SOAP`'s CCF to the master CCF in each wavelength bin and obtain the FWHM and depth values of the Gaussian from the best fit (Fig. C.1). The resulting values are fixed in `SOAP` configuration for each wavelength bin before the `emcee`-based fitting procedure used to determine R_P/R_*, u_1, and u_2 is executed.

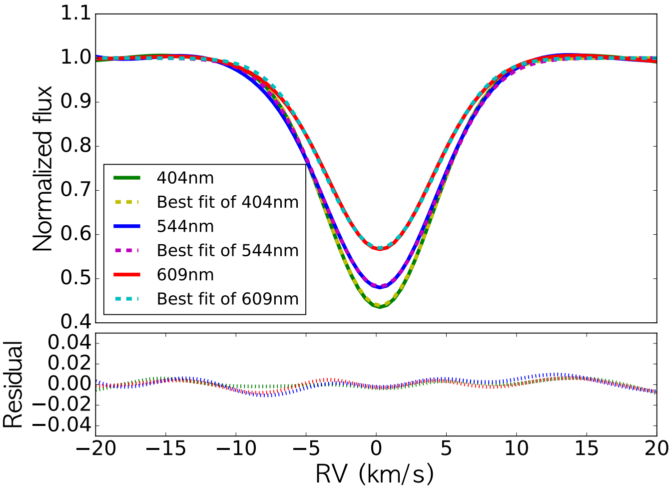

Fig. C.1. Example of the best fitted `SOAP` CCF to the master CCF in different wavelength bins, which leads to the determination of the Gaussian FWHM and depth parameters. The solid lines represent the master CCFs from the observations in the 440 nm (green), 544 nm (blue), and 609 nm (red) bins, respectively. The `SOAP` CCF resulting from the best-fit Gaussian parameters is shown by the dashed lines.

Appendix D: Posterior distributions

An example of the posterior distributions of the free parameters (R_P/R_*, u_1, u_2) resulting from the `emcee`-based fitting procedure is shown in Fig. D.1.

Appendix E: Comparison with non-SKYSUB data

In the results section we present the transmission spectra obtained from the ESPRESSO SKYSUB data set extracted by the DRS pipeline. However, we also tested the CHOCOLATE methodology on the non-SKYSUB ESPRESSO data set (Fig. E.1) to evaluate the impact of sky subtraction on the results. Consequently, we found that there is no meaningful impact on the results. Nevertheless, we obtained that the non-SKYSUB data set performed spuriously on the last bin.

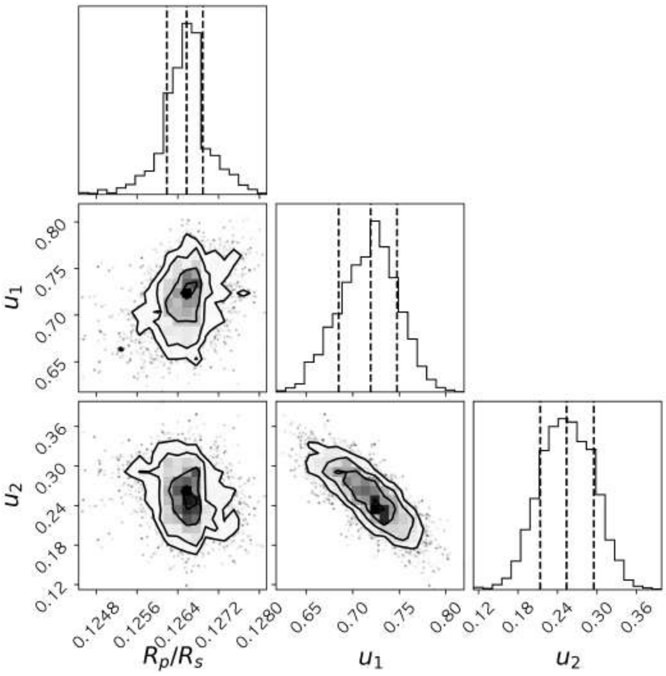

Fig. D.1. Posterior distributions obtained through the fitting procedure using the 528-nanometer-centered bin as an example. The central dashed line indicates the best-fit value of each fitting parameter. The surrounding dashed lines mark the 1σ values of each distribution, which were taken to be the value enclosed in the 68.3% of the posterior distributions.

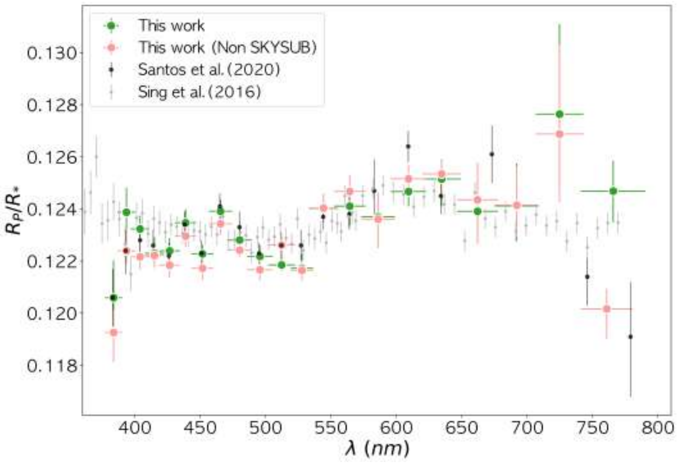

Fig. E.1. Comparison between transmission spectra of HD 209458b obtained from SKYSUB and non-SKYSUB data sets.

Appendix F: Results from separate nights

We show in Fig. F.1 the transmission spectra obtained by applying our analysis independently to Night 1 and Night 2 data sets, and we compare them with the results of our analysis obtained from the combined data set presented in Sect. 5. We find that in the case of HD209458 b, which is a quiet star, the combination of two observing nights is good enough to obtain a conclusive result. However, in the case of an active star, where the activity may differ between nights, a larger combination of data sets might be needed.

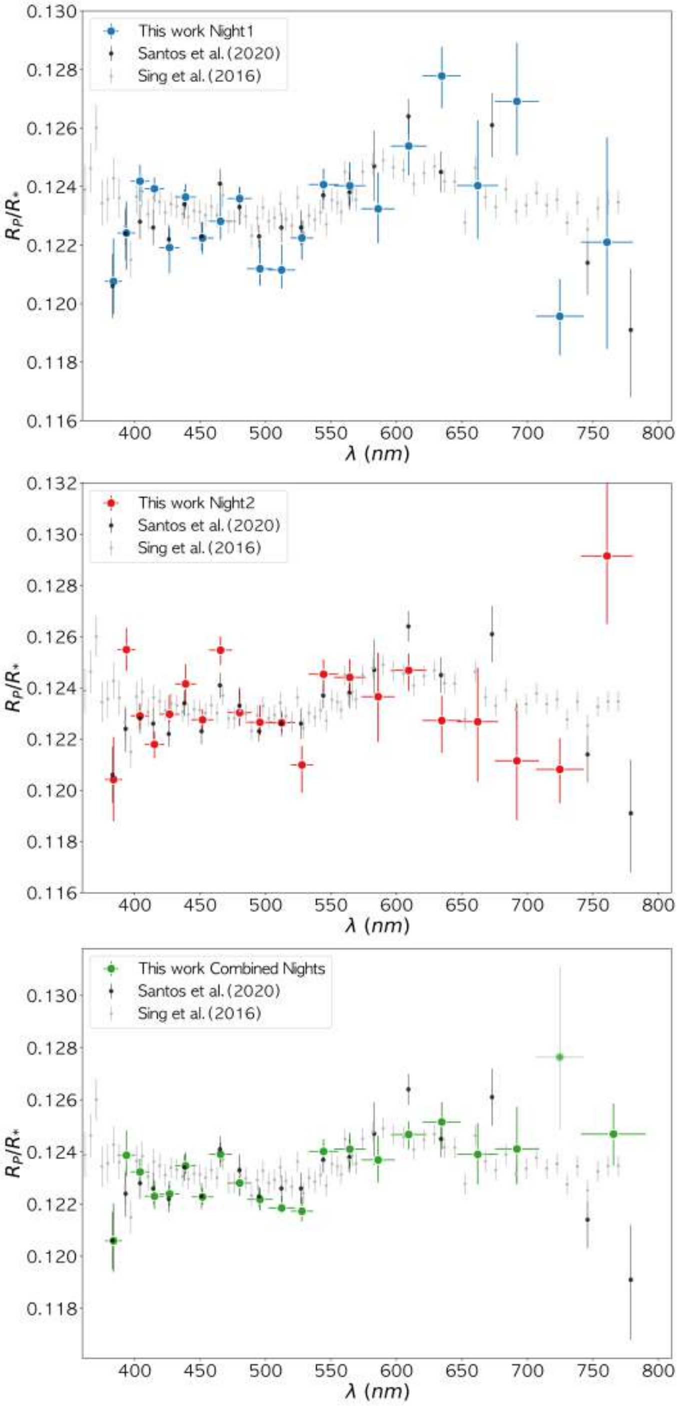

Fig. F.1. Transmission spectra of HD 209458b obtained from our analysis using Night 1 (top panel, blue circle), Night 2 (middle panel, red circle), and combined (bottom panel, green circle) data sets. Each result is compared to the transmission spectra obtained by Santos et al. (2020) (black circle) and Sing et al. (2016) (gray circle).